Pressure-Regulated Synthesis of Cu(TPA)·(DMF) in Microdroplets for Selective CO2 Adsorption

Journal:	*Dalton Transactions*
Manuscript ID	DT-ART-09-2018-003812.R3
Article Type:	Paper
Date Submitted by the Author:	12-Dec-2018
Complete List of Authors:	He, Xiang; Virginia Commonwealth University, Wang, Wei-Ning; Virginia Commonwealth University, Mechanical and Nuclear Engineering

Pressure-Regulated Synthesis of Cu(TPA)·(DMF) in Microdroplets for Selective CO_2 Adsorption

Xiang He and *Wei-Ning Wang*[*]

Department of Mechanical and Nuclear Engineering, Virginia Commonwealth University, Richmond, Virginia 23219, United States

*Email: wnwang@vcu.edu

ABSTRACT

The synthesis of metal-organic frameworks (MOFs) by using traditional wet-chemistry methods generally requires very long durations and still suffers from non-uniform heat and mass transfer within the bulk precursor solutions. Towards addressing these issues, a microdroplet-based spray method has been developed. In a typical spray process, the MOF's precursor solution is first atomized into microdroplets. These droplets serve as the microreactors to ensure homogeneous mixing, fast evaporation, and rapid nucleation and crystal growth to form MOF particles. However, the fundamental MOF formation mechanisms by using this strategy have not been fully understood. In this work, the role of the operating pressure in the synthesis of a representative MOF (i.e., Cu(TPA)·(DMF); TPA: terephthalic acid, DMF: dimethylformamide) was systematically investigated. Detailed characterization showed that the pressure variations significantly affected both the morphologies and crystalline structures of Cu(TPA)·(DMF). Numerical simulations revealed that the morphology changes are mainly attributed to the variations in supersaturation ratios, which are caused by different microdroplet evaporation rates due to the regulation of operating pressure. While the crystalline structure variations are closely related to the dissociation of DMF molecules at lower operating pressures. Besides, the dissociation of DMF molecules decreased the surface area of the MOF crystals, but gave rise to massive coordinatively unsaturated metal sites, which greatly enhanced the interaction of CO_2 with the MOF crystal and thus led to improved CO_2 adsorption capacity and selectivity. The outcome of this work would shed new light on the fundamental understanding of MOF synthesis using the microdroplet-based spray method.

KEYWORDS: *MOFs, spray, coordinatively unsaturated sites, selective CO_2 adsorption, IAST, virial equation*

INTRODUCTION

Metal-organic frameworks (MOFs), a family of porous polymer materials, are becoming a rising star in material science by virtue of their huge porosity, exceptional surface area, and tunable surface chemistry.[1-3] MOFs are constructed from metal ions/clusters and organic ligands. The abundance of various metal ions and organic linkers grants MOFs considerable diversity. Examples of typical MOF series include ZIFs (zeolitic imidazole frameworks),[4] UIOs (University of Oslo),[5] MILs (Materials of Institute Lavoisier),[6] and CAUs (Christian-Albrechts University).[7] Given the extraordinary properties of MOFs, they have been used in a broad range of applications, including gas separation,[8] gas storage,[9] catalysis,[10-11] water treatment,[12-13] sensing,[14] and biomedical applications.[15] MOFs can also be integrated with other materials (e.g., metals and semiconductors) to enhance their functionalities and efficiencies by boosting molecule adsorption, facilitating charge transfer, and promoting molecule activation.[16-19]

Conventionally, MOFs are synthesized through heating bulk precursor solutions via wet-chemistry processes (e.g., the solvothermal method), where the structure evolution takes place, including deprotonation, coordination, nucleation, and crystal growth.[3] The wet-chemistry methods, however, are usually plagued with long synthesis durations due to inhomogeneous mixing and slow heat transfer within the bulk precursor solutions. For example, in a typical solvothermal process, it generally takes hours even days to obtain well-crystallized ZIF-8 crystals.[20] Various forms of external energies have been used to assist the MOF synthesis, such as microwave irradiation,[21] ultrasound,[22] electric potential,[23] and mechanical force.[24] Recently, a microdroplet-based spray strategy was developed for the fast and high-throughput synthesis of MOFs.[25, 26] In a typical spray process, the MOF precursor solutions are firstly atomized into droplets with the size ranging from micrometers to millimeters. These droplets serve as

microreactors, where uniform mixing and fast heat transfer can be easily achieved to promote efficient deprotonation and coordination. The microdroplets are then subjected to heating for solvent evaporation, nucleation, and crystal growth to form the final MOFs crystals. The whole process only takes about several seconds to complete, making the spray route a rational strategy for the fast synthesis of MOFs. Besides, the spray method can also be used for the postsynthetic modification of MOFs,[27] manufacture of multicomponent MOF superstructures[25] and hierarchical MOFs.[28] It should be noted that, the synthesis of MOFs by using the spray method is still in its early stage. More work needs to be conducted to unravel the formation mechanism of MOFs in this rapid process.

In particular, the evaporation of microdroplets is the first and foremost step of the synthesis of MOFs by using the spray process, because the solvent evaporation of microdroplets directly influences the kinetics of supersaturation of precursors,[29] which will have great effects on the subsequent MOFs formation steps, i.e., nucleation and crystal growth.[3, 30] Fundamentally, the evaporation of microdroplets is a macroscopic phenomenon of microscopic heat and mass transfer,[31] which is generally controlled by several factors, including solvent types, operating temperature, and pressure. In a recent study, we studied the effect of operating temperature on the synthesis of $[Cu_3(TMA)_2(H_2O)_3]_n$ (TMA: trimesic acid) via the microdroplet-based spray method.[26] The results showed that, the operating temperature affected not only the crystal size but also the accessible open coordination sites. It should be noted that, $[Cu_3(TMA)_2(H_2O)_3]_n$ became amorphous under operating temperatures higher than 300 °C due to the disintegration of organic ligands. Compared with temperature, the adjustment of operating pressure is a milder way to regulate the synthesis of MOFs in microdroplets. Based on the previous studies of inorganic materials formation in microdroplets,[32-33] the regulation of operating pressure would

dramatically change the evaporation behaviors of microdroplets,[34] which will alter the supersaturation ratios, nucleation and crystal growth kinetics, and eventually gives rise to different properties of the final products. However, the role of operating pressure in the formation of MOFs in microdroplets has not yet been explored thus far.

Herein, the current work aims to investigate the effect of operating pressure on the formation of MOFs in microdroplets. To be specific, a spray process equipped with a pressure control system was built. A representative MOF, Cu(TPA)·(DMF) (TPA: terephthalic acid, DMF: dimethylformamide), was chosen and synthesized under different operating pressures ranging from 0.2 atm to 1 atm (**Scheme 1**). Systematic material characterizations and numerical simulations of microdroplets evaporation were conducted to investigate the changes in MOF's properties brought by the variation in operating pressure. The results showed that, the operating pressure has significant effects on the MOF in terms of morphology, chemical structure, and gas adsorption ability (**Scheme 1**). Based on the results, a reasonable mechanism was proposed to explain the dependence of MOF's properties on operating pressure. The results from this work would advance the understanding of MOFs' synthesis by using the spray strategy.

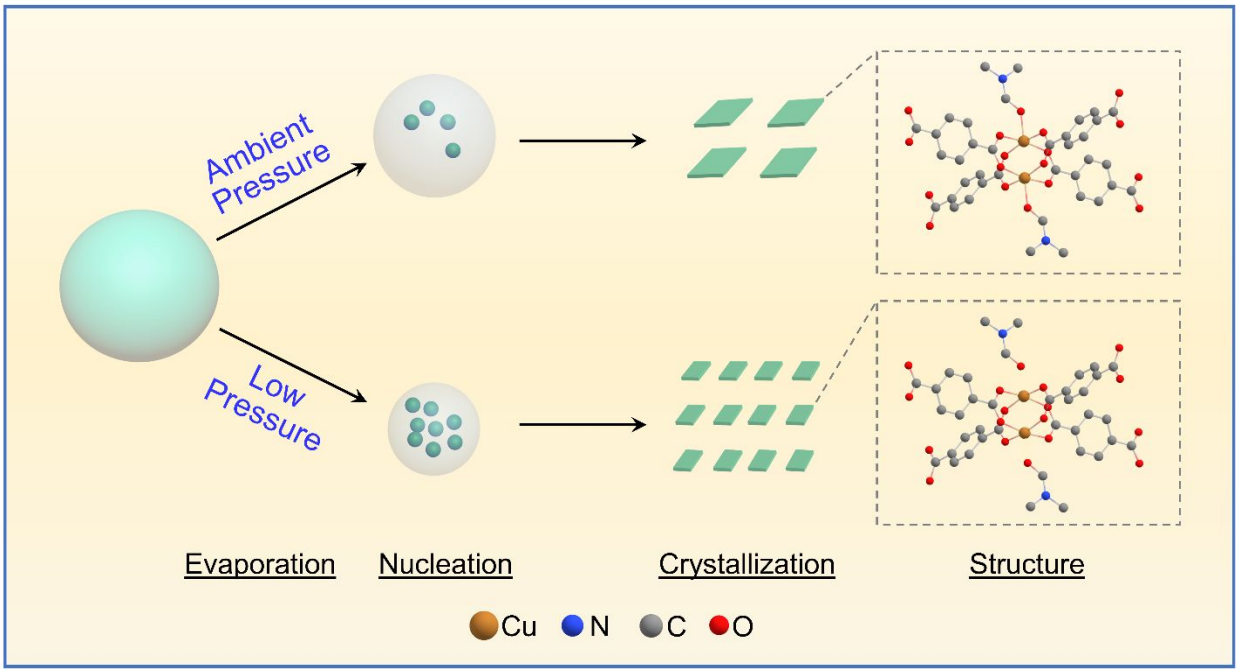

Scheme 1. Schematic illustration of the synthesis of Cu(TPA)·(DMF) in microdroplets under various operating pressures.

MATERIALS AND METHODS

Synthesis Process. As illustrated in **Scheme 2**, the microdroplet-based spray process is composed of several parts, including a Collison nebulizer, a tube furnace, a sample collector (i.e., microfiber filter) and a pressure control system. In a typical synthesis process, the precursor solution was firstly prepared by dissolving 0.2174 g $Cu(NO_3)_2{\cdot}3H_2O$ and 0.0997 g terephthalic acid (TPA) in 15 mL dimethylformamide (DMF). Subsequently, the precursor solution was nebulized into microdroplets, which were carried by an air flow (1.5 L/min) passing through the tube furnace at a pre-set temperature (200 °C). Flying through the furnace, the microdroplets underwent solvent evaporation, nucleation, and crystallization. The particles were finally collected by using the microfiber filter. During the spray process, the pressure inside the tube was adjusted within the range of 0.2 atm to 1 atm.

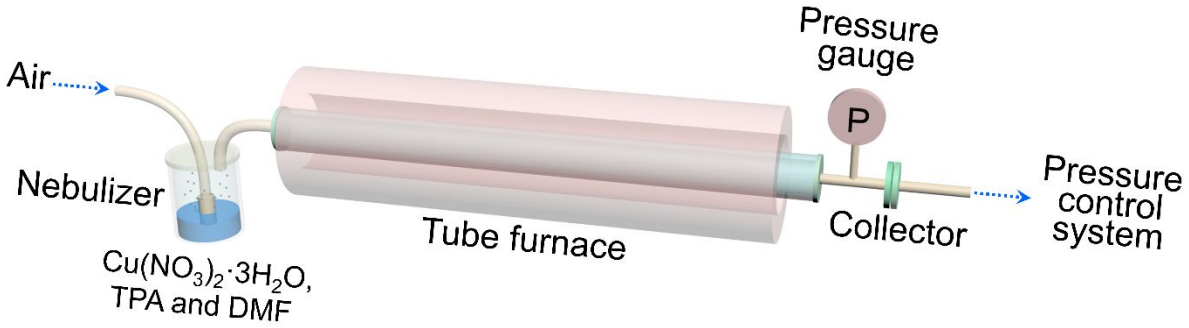

Scheme 2. Schematic illustration of the experimental set-up for the microdroplet-based synthesis of MOFs under various operating pressures.

Material Characterization. Detailed characterization of the as-synthesized samples was carried out by using scanning electron microscopy (SEM, Hitachi SU-70), X-ray powder diffraction (XRPD, PANalytical X'Pert Pro Diffractometer: Cu-Kα radiation source (λ = 1.5401Å);

reflection mode; step size = 0.026°; time per step: 27.54 s), Fourier-transform infrared spectroscopy (FT-IR, Thermo Scientific Nicolet iS50), Raman spectroscopy (Horiba LABRam Spectrometer), X-ray photoelectron spectroscopy (XPS, Thermofisher ESCALab 250), and surface area and pore structure analysis (Autosorb iQ).

Gas Sorption Analysis. Autosorb iQ was used to obtain the sorption isotherms of N_2 and CO_2 at 273 K and 298 K. After the measurements, the CO_2 adsorption isotherms at these two temperatures were fitted with the virial equation (**Eq. 1**) to calculate the isosteric heats of CO_2 adsorption (Q_{st}) (**Eq. 2**).[35-36]

$$ln\,(p) = ln(n) + \frac{1}{T}\sum_{i=0}^{A} a_i n^i + \sum_{i=0}^{B} b_i n^i \quad (1)$$

$$Q_{st} = -R\sum_{i=0}^{A} a_i n^i \quad (2)$$

where, p = gas pressure (Torr); n = amount of adsorbed gas molecules (mmol/g); T = temperature (K); a and b = virial coefficients with no dependence in temperature; Q_{st} = isosteric heat of adsorption (J/mol); R = gas constant (8.314 J/(K·mol)).

Analysis of CO_2/N_2 Adsorption Selectivity. The ideal adsorbed solution theory (IAST), which has been demonstrated to be an accurate method to predict gas adsorption selectivity in numerous prior studies,[37-39] was employed here to analyze the CO_2/N_2 adsorption selectivity of various Cu(TPA)·(DMF) samples. To be specific, the pure-component adsorption isotherms of CO_2 and N_2 were firstly fitted by using the dual-site (**Eq. 3**) and single-site (**Eq. 4**) Langmuir-Freundlich models, respectively.

$$q = q_{A,sat}\frac{c_A p^{\alpha_A}}{1 + c_A p^{\alpha_A}} + q_{B,sat}\frac{c_B p^{\alpha_B}}{1 + c_B p^{\alpha_B}} \quad (3)$$

$$q = q_{A,sat}\frac{c_A p^{\alpha_A}}{1 + c_A p^{\alpha_A}} \quad (4)$$

where, q = adsorption quantity (mmol/g); $q_{A,sat}$ and $q_{B,sat}$ = saturate adsorption quantities; subscripted A and B indicate various adsorption sites; c_A and c_B = Langmuir-Freundlich coefficients (bar$^{-\alpha}$, temperature-dependent); p = gas phase pressure (bar); α_A and α_B = dimensionless exponents.

Subsequently, the fitting parameters were incorporated into **Eq. 5** to calculate the mole fraction of individual component in the adsorbed phase.

$$\int_0^{P \cdot y1/x1} \frac{q_1}{P} dp = \int_0^{P \cdot y2/x2} \frac{q_2}{P} dp \quad (5)$$

where, P = total pressure (bar); x and y = mole fraction of gas component in the adsorbed and bulk phase, respectively; q = adsorption quantity (mmol/g); subscripted numbers were used to differentiate the gas components.

Finally, the adsorption selectivity (S_{ads}) was calculated using **Eq. 6**.

$$S_{ads} = \frac{x_1/y_1}{x_2/y_2} \quad (6)$$

RESULTS AND DISCUSSION

Morphology Characterization

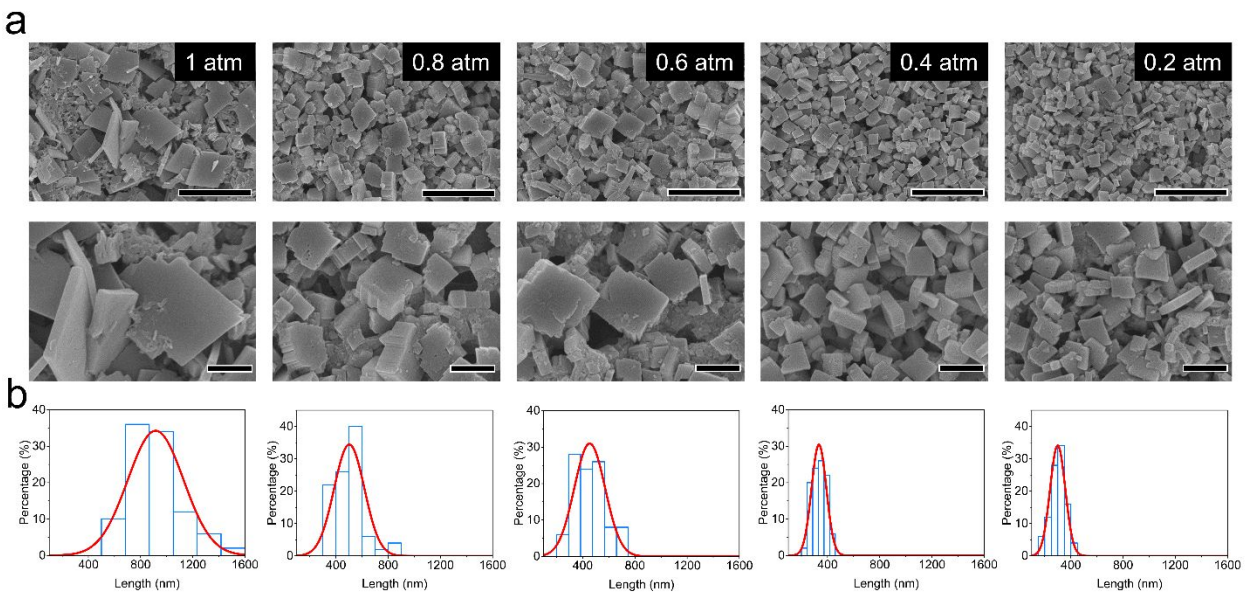

Figure 1. a) SEM images and b) size distribution histograms of Cu(TPA)·(DMF) synthesized under various pressures. Scale bars in SEM images: 2 μm (up) and 500 nm (down).

The Cu(TPA)·(DMF) samples synthesized under various pressures were subjected to detailed characterization. As exhibited in **Figure 1a**, all the Cu(TPA)·(DMF) samples synthesized by the spray process have a sheet morphology, which is consistent with the lamellar crystal structure of Cu(TPA)·(DMF).[40] Notably, the operating pressure affects the size distribution of Cu(TPA)·(DMF) (**Figure 1b**). And lower pressures give rise to smaller crystal sizes and more homogeneous size distributions. To be specific, the mean lengths of the Cu(TPA)·(DMF) crystals synthesized under 1, 0.8, 0.6, 0.4 and 0.2 atm were measured to be 915, 502, 453, 334 and 299 nm, respectively. Besides, Cu(TPA)·(DMF) crystals synthesized under ambient pressure (1 atm) have a wide size distribution, ranging from 400 nm to 1600 nm, while the size distribution becomes narrower with decreased pressures. The smaller size and narrow

size distribution under lower pressures can be ascribed to faster nucleation rate induced by rapid solvent evaporation. In addition, the operating pressure also has a significant effect on the length/thickness ratio of the samples. As shown in **Figure 2**, under ambient pressure, the Cu(TPA)·(DMF) exhibits the highest length/thickness ratio (~ 7.8). With the operating pressure smaller than 0.8 atm, the length/thickness ratio stabilizes around 2.6 to 3.4. The variations in crystal size, size distribution, and length/thickness ratio might be related to the pressure-modulated evaporation of the microdroplets during the spray process, as explained in detail in the following section.

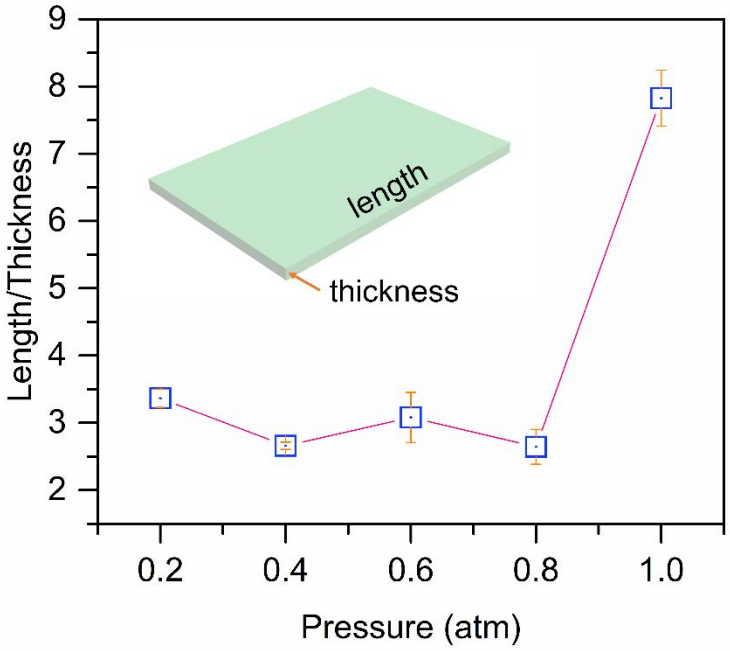

Figure 2. Effect of operating pressure on the length/thickness ratio of the samples.

Simulation of Microdroplet Evaporation

To better understand the dependence of microdroplet evaporation (i.e., droplet temperature and size) on the operating pressure, numerical simulations were carried out based on the fundamental heat and mass transfer principles.[41] The models are composed of four

differential equations (**Eqs 7-10**), describing the evolution of droplet diameter (D_d), solvent vapor concentration in air (n), droplet temperature (T_d), and air temperature (T_a) as a function of time, respectively. The assumptions are provided in supporting information, **S1.**

$$\frac{dD_d}{dt} = \frac{4D_v m_d(n - n_s)}{\rho_d D_d} \tag{7}$$

$$\frac{dn}{dt} = -2\pi D_d D_v N(n - n_s) \tag{8}$$

$$\frac{dT_d}{dt} = \frac{3L\frac{dD_d}{dt} + 6\frac{h_d}{\rho_d}(T_a - T_d)}{C_d D_d} \tag{9}$$

$$\frac{dT_a}{dt} = \frac{-\pi^2 R^2 {D_d}^2 N h_d(T_a - T_d) + 2\pi R h_t(T_t - T_a)}{FC_a} \times \frac{Q}{\pi R^2}\left(\frac{T_a}{T_a^0}\right)\left(\frac{1 - f_d^0}{1 - f_d}\right) \tag{10}$$

where D_d= droplet diameter (m), t = residence time (s), D_v = diffusion coefficient of DMF vapor (m^2/s, derived from **Eq. 11**[42]), m_d = molecule mass of DMF (kg), n = number concentration of DMF vapor molecules in air ($1/m^3$), n_s = saturated DMF vapor concentration ($1/m^3$), ρ_d = DMF density (kg/m^3), N = number density of microdroplets in air ($1/m^3$), T_d = temperature of microdroplets (K), K_m = mass transfer coefficient of DMF vapor (m/s), n_t =DMF vapor concentration at tube wall ($1/m^3$), L = latent heat of DMF evaporation (J/kg), h_d = heat transfer coefficient around microdroplets ($W/(m^2 \cdot K)$), T_a = air temperature (K), C_d = heat capacity of DMF ($J/(kg \cdot K)$), R = tube radius (m), h_t = heat transfer coefficient near the tube ($W/(m^2 \cdot K)$), F = mass flow rate of air (kg/s), C_a = heat capacity of air ($J/(kg \cdot K)$), Q = volume flow rate of air (m^3/s), f_d = mole fraction of DMF vapor in air. Superscripted "0" indicates the initial values.

$$D_v = \frac{2.66T_a^{1.5} \times 10^{-7}}{pM_{ad}^{0.5}\sigma_{ad}^2\Omega_D} \tag{11}$$

where $M_{ad} = \frac{2}{1/M_a + 1/M_d}$, M_a = molecular weight of air (g/mol), M_d = molecular weight of DMF (g/mol), $\sigma_{ad} = \frac{\sigma_a + \sigma_d}{2}$, σ_a = hard sphere diameter of air (Å), σ_d = hard sphere diameter of DMF (Å), Ω_D is almost unity.

DMF droplets with an initial diameter of 2 μm were selected for simulation. As shown in **Figures 3a** and **3b**, upon evaporation, the DMF vapor number density in air increased drastically with time, which also leads to the decrease in droplet diameter (**Figures 3c** and **3d**). Notably, a lower operating pressure would enhance the diffusion coefficient of DMF vapor (**Eq. 11**), which would fasten the droplet evaporation and thus give rise to a higher DMF vapor number density and a smaller droplet diameter. To be specific, at the evaporation time of 0.04 ms, the diameter of the microdroplets was calculated to be 1.64 μm under the operating pressure of 1 atm, but decreased to 1.44 μm under 0.2 atm. The rapid decrease in droplet diameter under lower operating pressures would significantly increase the concentration of reactants, and therefore result in faster increase in supersaturation ratio. As shown in **Figure S1**, the supersaturation ratio of the solute at 0.04 ms under 0.2 atm was 1.46 times of that under 1 atm. The increase in supersaturation ratio would drastically promote the nucleation process.[26] In particular, more seed nuclei can be obtained under lower operating pressures, which would yield smaller crystals. The simulation results are consistent with the SEM images (**Figure 1**). Meanwhile, a lower operating pressure also reduces the equilibrium temperature of the microdroplets (**Figure 3e** and **3f**). For instance, the equilibrium temperature of the droplet under 1 atm is 355 K, while the equilibrium temperature decreases to 329 K when process is operated under 0.2 atm. The results indicate that the evaporative cooling effect[34] becomes more

prominent under lower operating pressures, which will also make partial contributions to the increased supersaturation ratios.

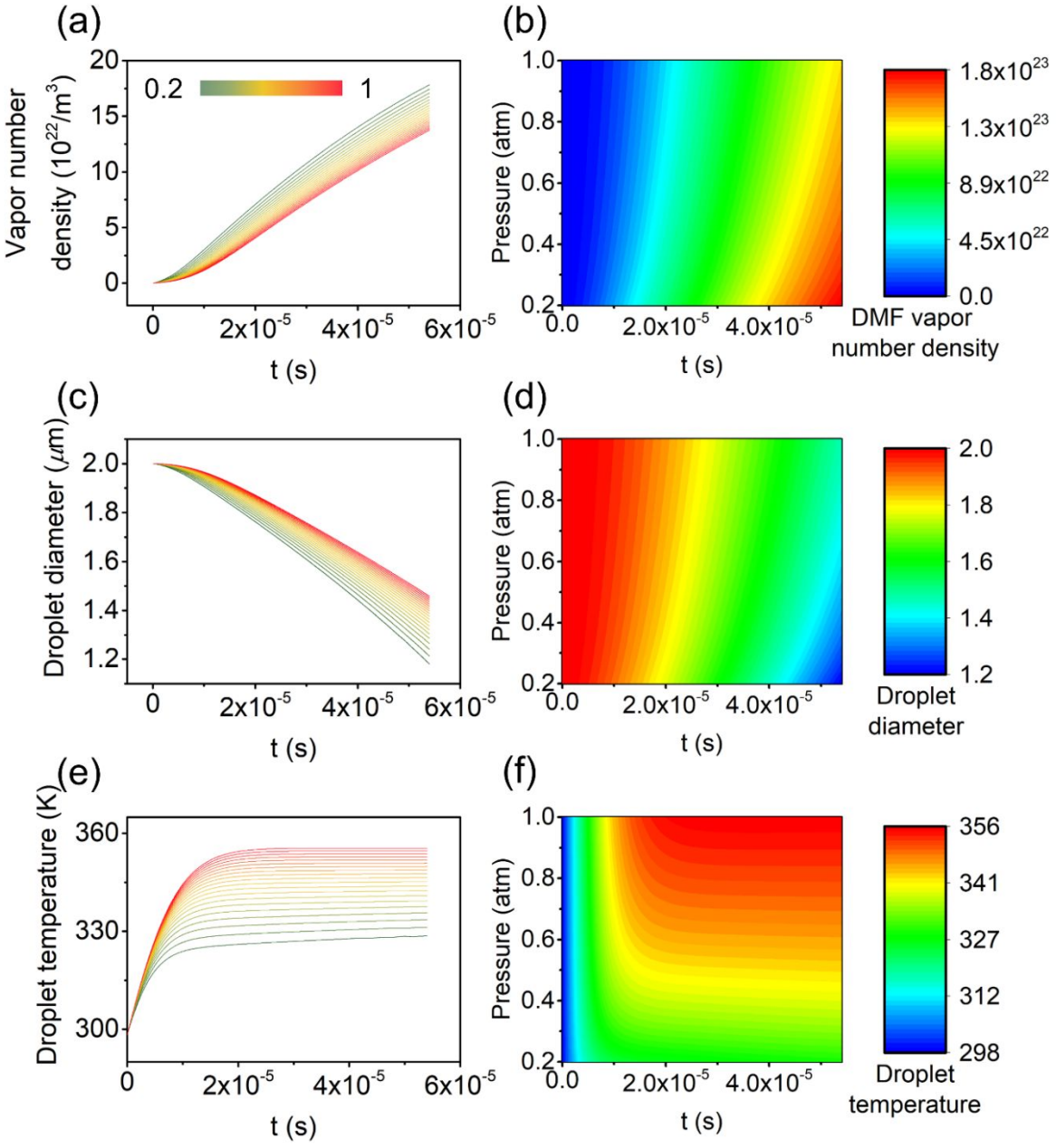

Figure 3. Evolution of DMF vapor density (a and b), droplet diameter (c and d), and droplet temperature (e and f) as a function of reaction time under various operating pressures. (a, inset) is the color bar used to indicate various operating pressures (unit: atm) for a, c, and e.

Chemical Properties Analysis

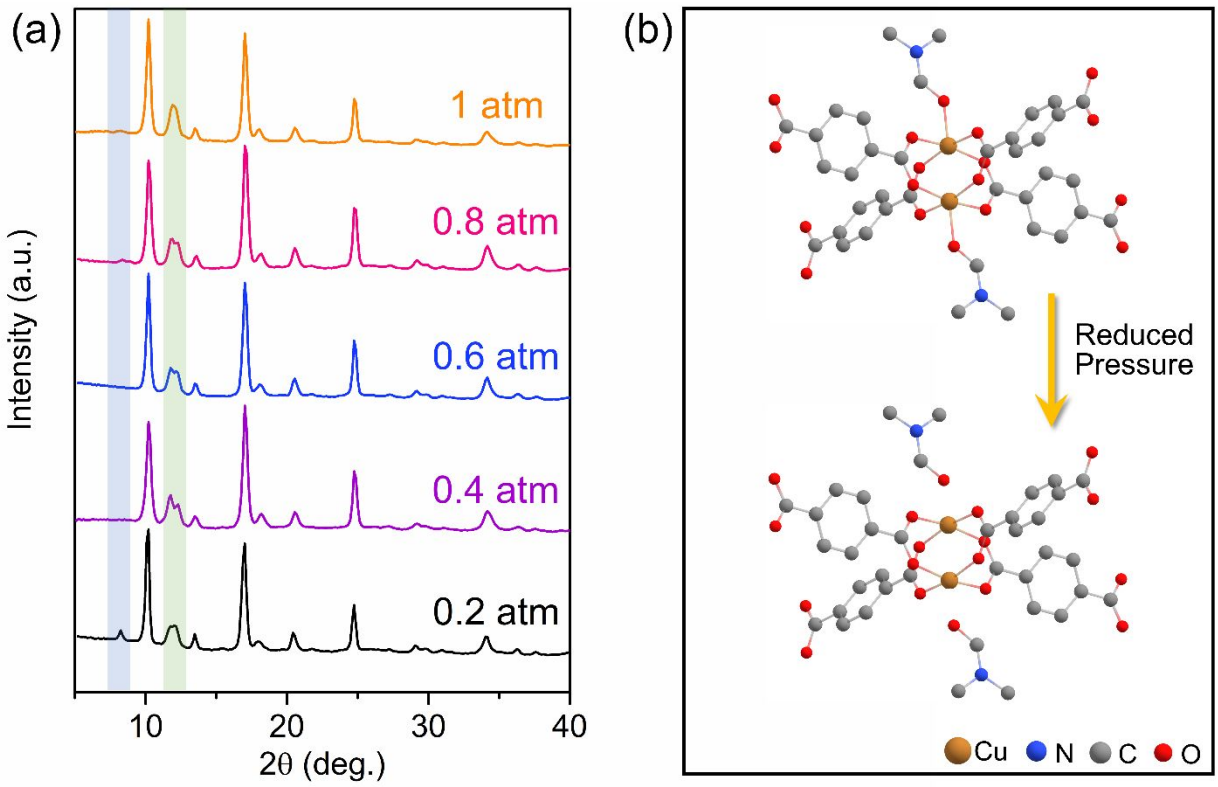

Figure 4. (a) XRPD patterns; (b) Schematic illustration of the effect of pressure on the crystal structure of Cu(TPA)·(DMF).

In addition to the morphology variations, the pressure also plays a significant role in the crystallinity of the products. As shown in **Figure 4a**, the XRPD patterns of the as-prepared samples agree well with the one reported previously.[40] The corresponding crystal structure (CCDC-687690)[40] of Cu(TPA)·(DMF) synthesized under 1 atm is illustrated in **Figure S2**. It is clear from the structure, the DMF molecules are coordinated with the Cu sites from one end, leaving the other end dangling inside the pores, which become vulnerable upon the variations of temperature and pressure during the synthesis process. Interestingly, with decreasing pressures, the diffraction peak at 12° gradually splits into two peaks. When synthesized at a very low

pressure (i.e., 0.2 atm), a new diffraction peak shows up at 8.2°. The variations in crystallinity may be attributed to the loss of DMF coordinated to Cu^{II} sites during the spray process under low-pressure conditions (**Figure 4b**), which is analogue to the temperature-modulated changes in crystal structures as reported previously.[40] Despite the various crystal structures, the samples synthesized under various pressures possess similar functional groups as demonstrated from the FT-IR (**Figure S3a**) and Raman spectra (**Figure S3b**). All the functional groups stem from the Cu(TPA)·(DMF) crystals.[40, 43] The assignments of the primary IR frequencies and Raman shifts are summarized in **Table 1**. For instance, the IR bands at 676, 1105, 1255, 1386, and 1663 cm^{-1} can be assigned to δ(OCN), $r(CH_3)$, υ_a(C'N), δ(CH) and υ(CO), respectively. All these peaks originate from the DMF molecules existed inside Cu(TPA)·(DMF) crystals. Compared with those of the free DMF molecules (**Figure S3a**), these peaks redshift a little bit to higher wavenumbers. The IR band at 1604 cm^{-1} corresponds to υ_a(COO) of TPA. More information was obtained from the Raman spectra (**Figure S3b**). In particular, the bands at the Raman shifts of 182 and 316 cm^{-1} can be ascribed to ν(Cu-Cu) and ν(Cu-O), respectively.

Table 1. The assignments of the representative IR wavenumbers and Raman shifts.

FT-IR		Raman	
Wavenumber (cm^{-1})	Assignment	Raman shift (cm^{-1})	Assignment
676	δ(OCN)	182	ν(Cu-Cu)
882	υ_s(C'N)	316	ν(Cu-O)
1105	$r(CH_3)$	1430	υ_s(COO)
1255	υ_a(C'N)	1609	ν(C=C)
1386	δ(CH)		
1439	$\delta_s(CH_3)$		
1604	υ_a(COO)		
1663	υ(CO)		

The surface elemental information of Cu(TPA)·(DMF) crystals synthesized under various pressures was examined through XPS measurements. As shown in **Figure S4**, all samples exhibit almost identical XPS spectra, including survey scans and high-resolution spectra. Primary elements in Cu(TPA)·(DMF) crystal were identified. In particular, the peaks at 932.5 eV and 952.5 eV can be assigned to Cu 2p3/2 and Cu 2p1/2, respectively.[16] While, the peaks center at 398.3 eV and 529.7 eV correspond to N 1s and O 1s, respectively.[44-45] The minimal differences in FTIR, Raman and XPS results among the samples indicate that, even though the DMF molecules are dissociated from the copper sites at low operating pressures, they might be still trapped inside the pores of the MOF crystals.

The dissociation of DMF from copper sites in Cu(TPA)·(DMF) samples also gives rise to the changes in other properties, including surface area and availability of coordinatively unsaturated copper sites. The surface area and pore size distribution of the samples were analyzed with nitrogen sorption experiments. In particular, the Brunauer–Emmett–Teller (BET) method was used to derive the surface areas (**S6**). The results show that Cu(TPA)·(DMF) sample synthesized at 1 atm (hereafter Cu(TPA)·(DMF)_1) has a BET surface area of 1187 m^2/g, while the one synthesized at 0.4 atm (hereafter Cu(TPA)·(DMF)_0.4) only has a BET surface area of 57 m^2/g. The nitrogen sorption isotherms of the samples are shown in **Figure 5**. For Cu(TPA)·(DMF)_1, the rapid increase in nitrogen uptake observed at low relative pressure (P/P_0 < 0.01) indicates the abundance of micropores, while the slight increase at high relative pressure and the existence of hysteresis suggest the presence of mesopores. For Cu(TPA)·(DMF)_0.4, similar nitrogen sorption isotherm was observed but with fewer micropores. The co-existence of mircopores and mesopores is also confirmed by the pore size distribution results. As shown in **Figures 5b** and **5d**, Cu(TPA)·(DMF)_1 and Cu(TPA)·(DMF)_0.4 exhibit similar pore size

distributions. Fewer micropores are observed in the case of Cu(TPA)·(DMF)_0.4, which is consistent with the nitrogen sorption isotherms. The change in the porous structures becomes more apparent when a lower pressure (0.2 atm) was used, where the sample was designated as Cu(TPA)·(DMF)_0.2. In particular, Cu(TPA)·(DMF)_0.2 has a BET surface area of 49 m^2/g, with a dominated pore diameter of 27.7 Å.

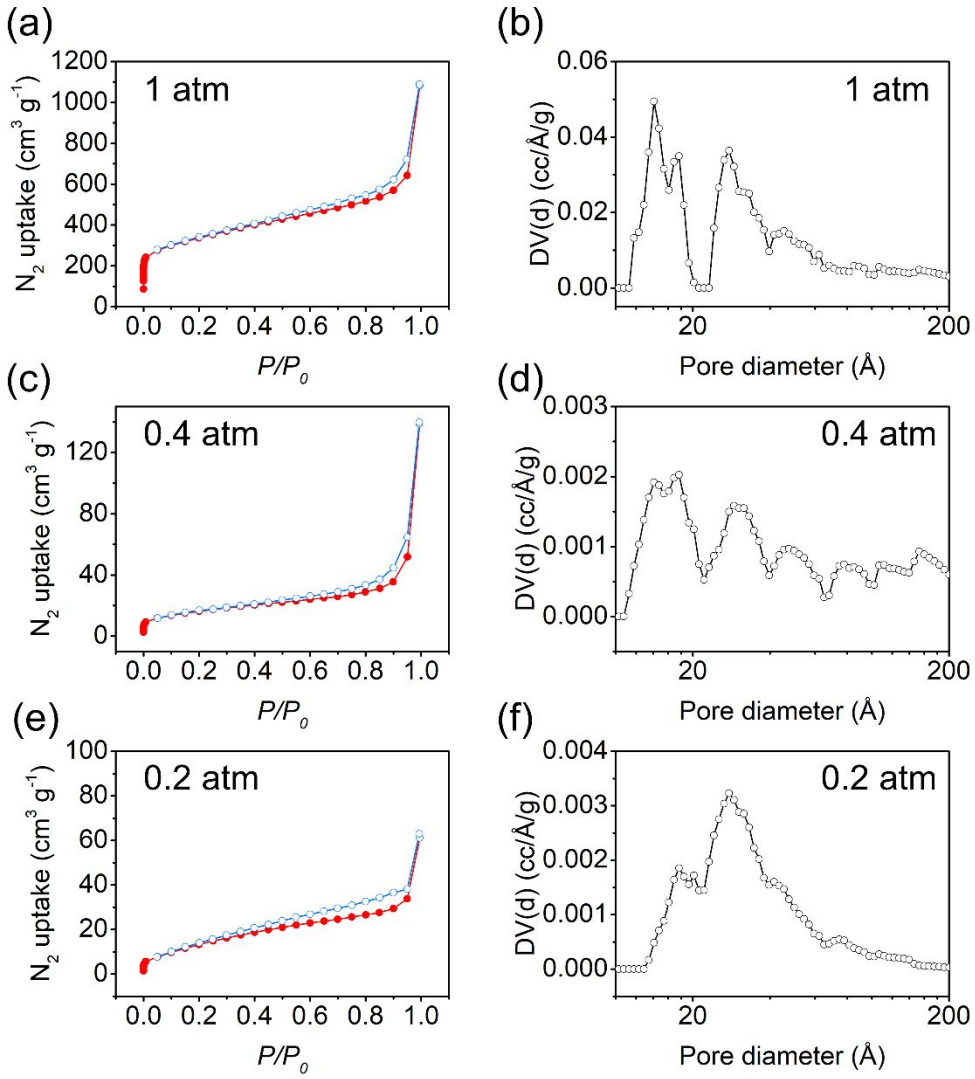

Figure 5. Nitrogen sorption isotherms and Density Functional Theory (DFT) pore size distributions of Cu(TPA)·(DMF) synthesized under various pressures (NLDFT-N_2-carbon equilibrium transition kernel at 77 K based on a slit-pore model).

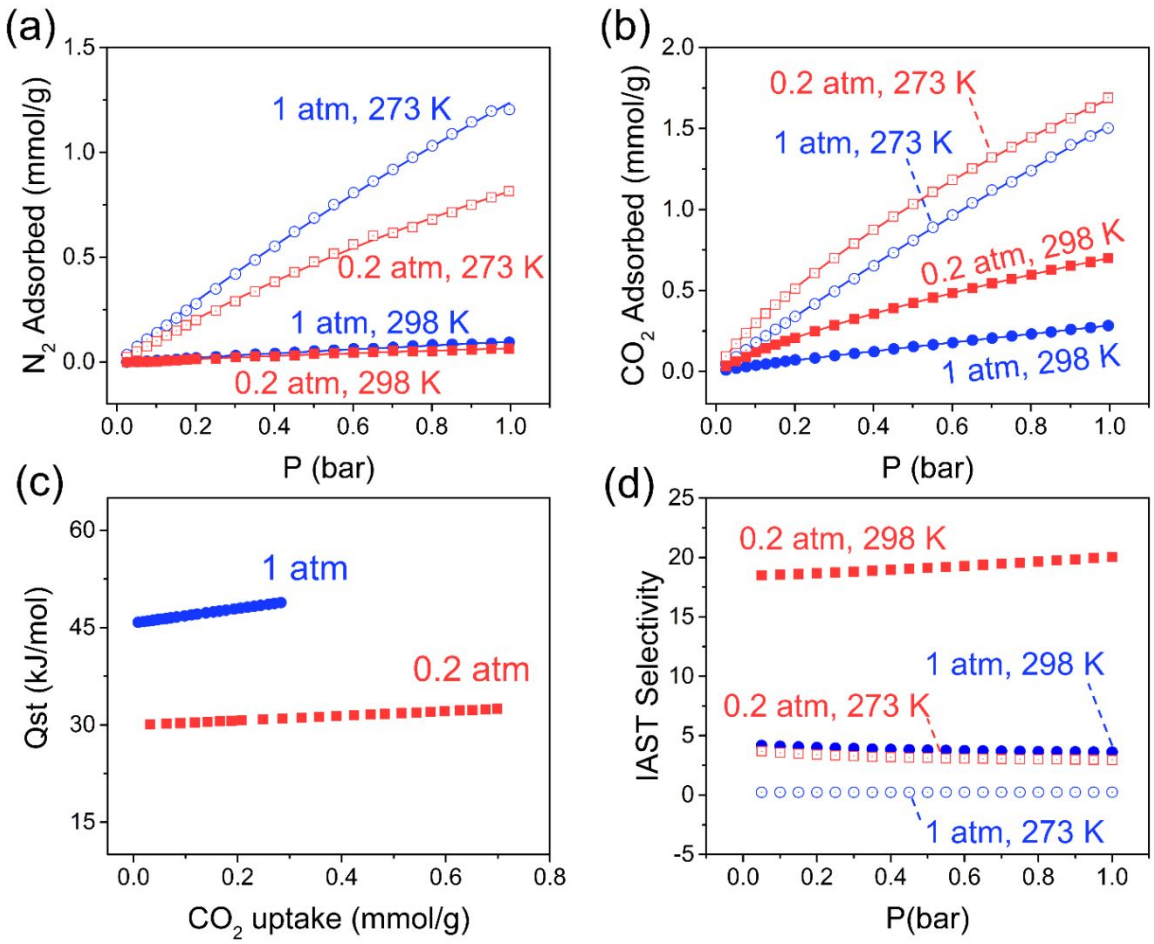

Figure 6. (a) N_2 adsorption isotherms; (b) CO_2 adsorption isotherms; (c) Isosteric heats of CO_2 adsorption; (d) Adsorption selectivity for CO_2/N_2 mixtures estimated using IAST. Note: the pressure values indicate the operating pressures used during the synthesis process; the temperature values indicate the temperatures used for gas adsorption tests.

The variations in porosity and crystal structures of Cu(TPA)·(DMF) lead to different performances in gas adsorption as demonstrated with N_2 and CO_2 adsorption experiments (**Figure 6**). The analysis of pure gas adsorption was performed at 273 K and 298 K, after which, in-depth modelling was conducted to analyze the isosteric heats and adsorption selectivity. Specifically, at 273 K, Cu(TPA)·(DMF)_1 has a N_2 uptake of 1.23 mmol/g at 1.0 bar, which is 52% higher than that of Cu(TPA)·(DMF)_0.2 (**Figure 6a**). While, at a higher temperature (298 K), these two samples possess similar N_2 adsorption capacity (~ 0.10 mmol/g at 1.0 bar).

Interestingly, Cu(TPA)·(DMF)_0.2 shows much higher capacity for CO_2 uptake at both 273 K and 298 K (**Figure 6b**), even though the surface area of Cu(TPA)·(DMF)_0.2 is much smaller than that of Cu(TPA)·(DMF)_1. To get further understanding of the CO_2 adsorption with these two samples, the isosteric heats of CO_2 adsorption were calculated using the Clausius-Clapeyron equation (**Eq. 2**). In the case of Cu(TPA)·(DMF)_1, the isosteric heats of CO_2 adsorption gradually increased with higher loading of CO_2, which might arise from the enhanced CO_2-CO_2 interaction.[37] Compared with isosteric heats of CO_2 adsorption for Cu(TPA)·(DMF)_0.2 (~ 30 kJ/mol), higher values were observed with Cu(TPA)·(DMF)_1 (46 to 49 kJ/mol), which indicates that the interaction between CO_2 molecules and Cu(TPA)·(DMF)_1 was stronger than that with Cu(TPA)·(DMF)_0.2. Besides, it also suggests tunability of isosteric heats of CO_2 adsorption through pressure-regulated synthesis of Cu(TPA)·(DMF) samples, offering huge potentials to optimize sorption profiles of CO_2. As shown in **Table 2**, the isosteric heats of CO_2 adsorption of the Cu(TPA)·(DMF) are comparable with other porous materials, such as $Cu_3(BTC)_2$ (29.8 ± 0.2 kJ/mol), Mg-MOF-74 (22 to 42 kJ/mol)), and zeolites (20 to 50 kJ/mol). It should be noted that the isosteric heats of CO_2 adsorption of Cu(TPA)·(DMF) samples can be further improved by modifying binding functionalities, just like the examples exhibited in **Table 2** (i.e., cation-exchanged MCM-22 zeolite and modified SBA-15 mesoporous silica). In addition, the IAST model was used to analyze the adsorption selectivity for CO_2 from flue gas (75% N_2, 15% CO_2 and 10% other gases) based on the isotherms (see **Experimental** section for details). As shown in **Figure 6d**, the IAST selectivities of Cu(TPA)·(DMF)_0.2 at 273 K and 298 K are calculated to be ~ 3 and ~ 20, respectively, which are much larger than those of Cu(TPA)·(DMF)_1, indicating that Cu(TPA)·(DMF)_0.2 has a better ability to selectively adsorb CO_2 over N_2.

Table 2. Comparison of the isosteric heats of adsorption

Adsorbate	Adsorbent	Q_{st} (kJ/mol)	Reference
CO_2	Cu(TPA)·(DMF)_0.2	~ 30	this work
CO_2	Cu(TPA)·(DMF)_1	46 to 49	this work
CO_2	$Cu_3(BTC)_2$	29.8 ± 0.2	49
CO_2	Mg-MOF-74	22 to 42	50
CO_2	CMP-1	24 to 26	51
CO_2	ZK-5	25 to 50	52
CO_2	Cation-exchanged MCM-22 zeolite	20 to 40	53
CO_2	Modified SBA-15 mesoporous silica	10 to 70	54

Note: BTC: Benzene-1,3,5-tricarboxylic acid; CMP: conjugated microporous polymer; ZK-5: an 8-membered-ring zeolite (Framework Type Code: KFI).

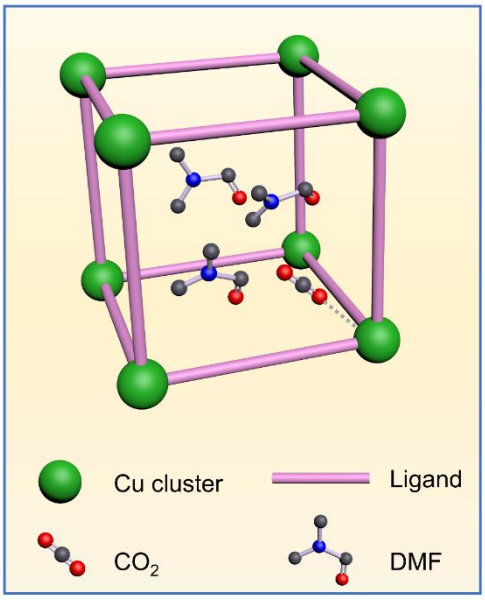

Scheme 3. Schematic illustration of CO_2 adsorption inside the framework of Cu(TPA)·(DMF) synthesized under low pressures. H atoms are omitted for simplicity.

On the basis of the above results, a plausible mechanism for the enhanced CO_2 uptake and selectivity with Cu(TPA)·(DMF)_0.2 was schematically illustrated in **Scheme 3**. With lower operating pressures, DMF molecules tend to dissociate from the crystal structure due to the increased diffusivity of DMF molecules (**Eq. 11**). Instead of leaving away from the framework, these dissociated DMF molecules are trapped inside the pores as suggested by the systematic characterization results (**Figures 4a, S3**, and **S4**). The dissociated but trapped DMF molecules led to decreased surface area but created massive coordinatively unsaturated copper sites. As demonstrated in many prior studies,[46-47] the coordinatively unsaturated metal sites would produce strong electric fields to bind polar molecules (e.g., CO_2),[48] which would subsequently improve the CO_2 adsorption capacity. Generally, the open metal sites would also increase the isosteric heat (Qst). However, smaller Qst values were observed for Cu(TPA)·(DMF)_0.2 compared with that for Cu(TPA)·(DMF)_1. This might be due to the fact that, Cu(TPA)·(DMF)_0.2 has lots of dissociated DMF molecules trapped inside the pores (**Scheme 3**), which would cause steric hindrance and thus decrease the isosteric heat.

CONCLUSIONS

A pressure-regulated microdroplet-based spray route has been developed for the synthesis of MOFs. Systematic experimental and modelling studies have been conducted to investigate the dependence of the properties of Cu(TPA)·(DMF) on the pressures of the spray process. Apparent variations in morphology and crystal structure were observed with different synthesis pressures, which could be attributed to the different evaporation rates of microdroplets and the dissociation of coordinated DMF under low pressures, respectively. The dissociation of DMF molecules would generate large numbers of coordinatively unsaturated metal sites, which leads to higher CO_2 adsorption capacity and selectivity. The outcome of this work would contribute to the fundamental understanding of pressure-regulated synthesis of MOFs using spray process.

ASSOCIATED CONTENT

Assumptions for the simulation of microdroplet evaporation; Calculation of the supersaturation ratio; Crystal structure of Cu(TPA)·(DMF) synthesized under 1 atm; FTIR and Raman spectra of Cu(TPA)·(DMF) synthesized under various pressures; XPS spectra of Cu(TPA)·(DMF) synthesized under various pressures; Determining surface areas of MOFs using the BET method.

AUTHOR INFORMATION

Corresponding Author

*Wei-Ning Wang: Tel: 1-(804) 827-4306; Fax: 1-(804) 827-7030; Email: wnwang@vcu.edu

Notes

The authors declare no competing financial interest.

ACKNOWLEDGMENT

Financial support from the National Science Foundation (CMMI-1727553) is gratefully acknowledged.

REFERENCES

1. L. Zhu, X.-Q. Liu, H.-L. Jiang and L.-B. Sun, *Chemical Reviews*, 2017, **117**, 8129-8176.
2. E. M. Dias and C. Petit, *J Mater Chem A*, 2015, **3**, 22484-22506.
3. N. Stock and S. Biswas, *Chem Rev*, 2012, **112**, 933-969.
4. R. Banerjee, H. Furukawa, D. Britt, C. Knobler, M. O'Keeffe and O. M. Yaghi, *J Am Chem Soc*, 2009, **131**, 3875-3877.
5. M. Kandiah, M. H. Nilsen, S. Usseglio, S. Jakobsen, U. Olsbye, M. Tilset, C. Larabi, E. A. Quadrelli, F. Bonino and K. P. Lillerud, *Chem Mater*, 2010, **22**, 6632-6640.
6. G. Ferey, C. Serre, C. Mellot-Draznieks, F. Millange, S. Surble, J. Dutour and I. Margiolaki, *Angew Chem Int Edit*, 2004, **43**, 6296-6301.
7. T. Ahnfeldt, N. Guillou, D. Gunzelmann, I. Margiolaki, T. Loiseau, G. Ferey, J. Senker and N. Stock, *Angew Chem Int Edit*, 2009, **48**, 5163-5166.
8. F. Cacho-Bailo, G. Caro, M. Etxeberria-Benavides, O. Karvan, C. Tellez and J. Coronas, *Chem Commun*, 2015, **51**, 11283-11285.
9. I. Spanopoulos, C. Tsangarakis, E. Klontzas, E. Tylianakis, G. Froudakis, K. Adil, Y. Belmabkhout, M. Eddaoudi and P. N. Trikalitis, *J Am Chem Soc*, 2016, **138**, 1568-1574.
10. M. B. Majewski, A. W. Peters, M. R. Wasielewski, J. T. Hupp and O. K. Farha, *ACS Energy Lett*, 2018, **3**, 598-611.
11. H. G. T. Nguyen, N. M. Schweitzer, C.-Y. Chang, T. L. Drake, M. C. So, P. C. Stair, O. K. Farha, J. T. Hupp and S. T. Nguyen, *ACS Catal*, 2014, **4**, 2496-2500.
12. M. Mon, R. Bruno, J. Ferrando-Soria, D. Armentano and E. Pardo, *J Mater Chem A*, 2018, **6**, 4912-4947.
13. D. W. Wang, S. E. Gilliland, X. B. Yi, K. Logan, D. R. Heitger, H. R. Lucas and W. N. Wang, *Environ Sci Technol*, 2018, **52**, 4275-4284.
14. G. Lu and J. T. Hupp, *J. Am. Chem. Soc.*, 2010, **132**, 7832-7833.
15. T. Simon-Yarza, A. Mielcarek, P. Couvreur, and C. Serre, *Adv Mater*, **30**, 1707365.
16. X. He and W.-N. Wang, *J Mater Chem A*, 2018, **6**, 932-940.
17. X. He, C. Yang, D. Wang, S. E. Gilliland Iii, D.-R. Chen and W.-N. Wang, *CrystEngComm*, 2017, **19**, 2445-2450.
18. X. He, V. Nguyen, Z. Jiang, D. Wang, Z. Zhu and W.-N. Wang, *Catal Sci Technol*, 2018, **8**, 2117-2123.
19. D. Wang, Z. Li, J. Zhou, H. Fang, X. He, P. Jena, J.-B. Zeng and W.-N. Wang, *Nano-Micro Lett*, 2017, **10**, 4.
20. S. R. Venna, J. B. Jasinski and M. A. Carreon, *J Am Chem Soc*, 2010, **132**, 18030-18033.
21. I. Thomas-Hillman, A. Laybourn, C. Dodds and S. W. Kingman, *J Mater Chem A*, 2018, **6**, 11564-11581.
22. W.-J. Son, J. Kim, J. Kim and W.-S. Ahn, *Chem Commun*, 2008, DOI: 10.1039/B814740J, 6336-6338.
23. R. Ameloot, L. Stappers, J. Fransaer, L. Alaerts, B. F. Sels and D. E. De Vos, *Chem Mater*, 2009, **21**, 2580-2582.
24. T. Friscic, *J Mater Chem*, 2010, **20**, 7599-7605.
25. A. Carné-Sánchez, I. Imaz, M. Cano-Sarabia and D. Maspoch, *Nature Chem*, 2013, **5**, 203-211.
26. X. He, Z. Gan, S. Fisenko, D. Wang, H. M. El-Kaderi and W.-N. Wang, *ACS Appl Mater Inter*, 2017, **9**, 9688-9698.

27. L. Garzón-Tovar, S. Rodríguez-Hermida, I. Imaz and D. Maspoch, *J Am Chem Soc*, 2017, **139**, 897-903.
28. A. Garcia Marquez, P. Horcajada, D. Grosso, G. Ferey, C. Serre, C. Sanchez and C. Boissiere, *Chem Commun*, 2013, **49**, 3848-3850.
29. W. N. Wang, I. W. Lenggoro and K. Okuyama, in *Encyclopedia of Nanoscience and Nanotechnology*, ed. H. S. Nalwa, American Scientific Publishers, 2011, vol. 21, pp. 435-458.
30. J. Cravillon, C. A. Schroder, R. Nayuk, J. Gummel, K. Huber and M. Wiebcke, *Angew Chem Int Edit*, 2011, **50**, 8067-8071.
31. N. A. Fuchs, *The Mechanics of Aerosols*, Pergamon, Oxford, U.K., 1964.
32. W.-N. Wang, I. W. Lenggoro and K. Okuyama, *J Colloid Interf Sci*, 2005, **288**, 423-431.
33. W. Widiyastuti, R. Balgis, F. Iskandar and K. Okuyama, *Chem Eng Sci*, 2010, **65**, 1846-1854.
34. S. P. Fisenko, W. N. Wang, I. W. Lenggoro and K. Okyuama, *Chem Eng Sci*, 2006, **61**, 6029-6034.
35. L. Czepirski and J. JagieŁŁo, *Chem Eng Sci*, 1989, **44**, 797-801.
36. A. K. Sekizkardes, T. İslamoğlu, Z. Kahveci and H. M. El-Kaderi, *J Mater Chem A*, 2014, **2**, 12492-12500.
37. J. A. Mason, K. Sumida, Z. R. Herm, R. Krishna and J. R. Long, *Energy Environ Sci*, 2011, **4**, 3030-3040.
38. K. Sumida, D. L. Rogow, J. A. Mason, T. M. McDonald, E. D. Bloch, Z. R. Herm, T.-H. Bae and J. R. Long, *Chem Rev*, 2012, **112**, 724-781.
39. R.-J. Li, M. Li, X.-P. Zhou, D. Li and M. O'Keeffe, *Chem Commun*, 2014, **50**, 4047-4049.
40. C. G. Carson, K. Hardcastle, J. Schwartz, X. Liu, C. Hoffmann, R. A. Gerhardt and R. Tannenbaum, *Eur J Inorg Chem*, 2009, **2009**, 2338-2343.
41. Y. Xiong and T. T. Kodas, *J Aerosol Sci*, 1993, **24**, 893-908.
42. B. E. Poling, J. M. Prausnitz, O. C. John Paul and R. C. Reid, *The properties of gases and liquids*, McGraw-Hill New York, 2001.
43. K. Tan, N. Nijem, P. Canepa, Q. Gong, J. Li, T. Thonhauser and Y. J. Chabal, *Chem Mater*, 2012, **24**, 3153-3167.
44. H. Cao, X. Zhou, Z. Qin and Z. Liu, *Carbon*, 2013, **56**, 218-223.
45. G. Zhao, H. Hu, M. Deng and Y. Lu, *Chem Commun*, 2011, **47**, 9642-9644.
46. P. D. C. Dietzel, V. Besikiotis and R. Blom, *J Mater Chem*, 2009, **19**, 7362-7370.
47. E. J. García, J. P. S. Mowat, P. A. Wright, J. Pérez-Pellitero, C. Jallut and G. D. Pirngruber, *J Phys Chem C*, 2012, **116**, 26636-26648.
48. A. Ö. Yazaydın, A. I. Benin, S. A. Faheem, P. Jakubczak, J. J. Low, R. R. Willis and R. Q. Snurr, *Chem Mater*, 2009, **21**, 1425-1430.
49. C. R. Wade and M. Dincă, *Dalton T*, 2012, **41**, 7931-7938.
50. D. A. Yang, H. Y. Cho, J. Kim, S. T. Yang and W. S. Ahn, *Energy & Environmental Science*, 2012, **5**, 6465-6473.
51. R. Dawson, D. J. Adams and A. I. Cooper, *Chem Sci*, 2011, **2**, 1173-1177.
52. Q. Liu, T. Pham, M. D. Porosoff and R. F. Lobo, *Chemsuschem*, 2012, **5**, 2237-2242.
53. A. Zukal, J. Pawlesa and J. Čejka, *Adsorption*, 2009, **15**, 264-270.
54. V. Zeleňák, M. Skřínska, A. Zukal and J. Čejka, *Chem Eng J*, 2018, **348**, 327-337.

TABLE OF CONTENTS GRAPHIC